

A TDM-based Analog Front-End for Ear-EEG Recording with 83-G Ω Input Impedance, 384-mV DC Tolerance and 0.47- μ V_{rms} Input-Referred Noise

Huiyong Zheng, Yukun Ding, Xiao Liu

School of Information Science and Technology, Fudan University

State Key Laboratory of Integrated Chips and Systems, Fudan University, Shanghai 201203, China

Email: xiao@fudan.edu.cn

Abstract—This paper presents the design of a time-division multiplexed capacitively-coupled chopper analog front end with a novel impedance boost loop (IBL) and a novel DC servo loop (DSL). The proposed IBL boosts the input impedance of the analog front end to up to several tens of G Ω . It firstly utilizes an external IBL to prevent the total input impedance from degradation caused by parasitic capacitance from the ESD pad and external interconnections, and secondly relies on an internal IBL to compensate for the leakage current introduced by the chopper. The proposed DSL consists of a coarse DSL driven by square waveforms and a fine DSL driven by five phase-interleaving PWM waveforms, which up modulate the harmonics 5 times higher. An edge-pursuit comparator (EPC) is utilized to monitor the residual electrode offset voltage (EDO) at the LNA’s output. Designed in a 0.18- μ m CMOS process, the AFE consumes 4.5 μ A from a 1.2-V supply. The simulated input referred noise is 0.47 μ V_{rms} from 0.5 to 100 Hz in the presence of a 384-mV EDO. The proposed AFE achieves a high input impedance of 83 G Ω at 1 Hz and 9.3 G Ω at 100 Hz even with the presence of 20-pF parasitic capacitance.

Index Terms—chopper amplifier, dc servo loop, input impedance, low noise, time-division-multiplexing.

I. INTRODUCTION

EEG (Electroencephalogram) has been widely used for monitoring of various neurological disorders such as epilepsy and strokes [1]. However, EEG recording from the scalp takes a long time to set up and the procedure is usually carried out by trained professionals. The recording front-end is connected to electrodes via long cables, making it sensitive to motion artifacts. Hence, scalp-EEG recording is not suitable for day-to-day use outside a laboratory environment [2].

In contrast to scalp-EEG, ear-EEG is recorded in the outer ear or ear canal. Compared to scalp EEG, skins near ear are not covered by hair, offering a simple and comfortable electrode-skin interface. In addition, the ear offers a unique biological structure for hosting a miniaturized recording unit which can be either hidden in the ear canal or hooked onto the ear. Therefore, ear-EEG has great potential to be used for long-term monitoring applications. At present, ear-EEG has been used in sleep stage classification [3], hearing threshold test [4] and some other medical applications. It has also been used in a series of brain-computer interfaces, such as game control, motion imagination [5], biometric recognition, and self-modulated brain activity classification [6]. However, the ear-EEG signal’s amplitude is 10-15 dB smaller than the traditional scalp EEG [1], which

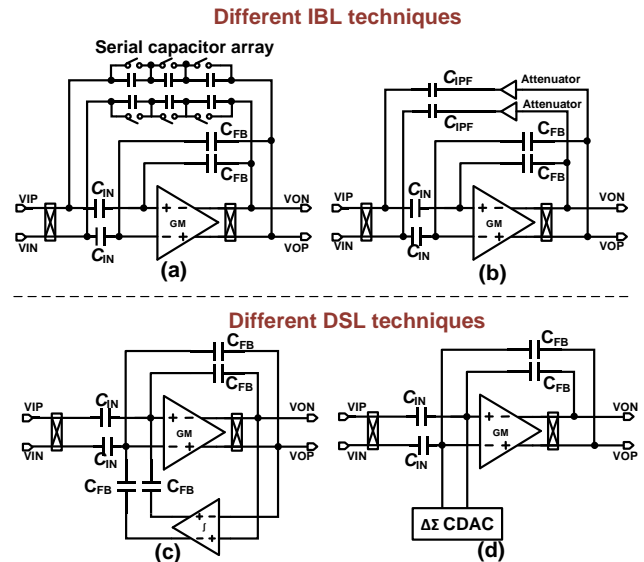


Fig. 1. (a) IBL with a serial capacitor array. (b) IBL with an attenuate amplifier. (c) DSL with an analog-mode integrator. (d) DSL with a delta-sigma CDAC.

increases the noise requirement of the analog front-end.

For the convenience of daily use, wearable ear-EEG uses dry electrodes [7]. The large electrode impedance of dry electrodes, in the range of a few hundreds of k Ω to a few tens of M Ω [1] leads to the loss of the effective input signal and the reduction of the signal to noise ratio (SNR). Conventional recording circuits used positive capacitive feedbacks to boost the input impedance [8]. However, parasitic capacitors associated with the feedback capacitors limit the impedance boost factor (IBF). In order to trim the positive feedback, Ha replaced the fixed feedback capacitor with a serial capacitor array as shown in Fig. 1(a) [9]. However, the improvement to the IBF is still limited due to the presence of parasitic capacitance in the switches. In [10], an attenuator amplifier is employed to reduce the resolution requirement of the capacitor array (C_{IPF}) as shown in Fig. 1(b). However, the attenuator amplifier contributes considerable noise to the system.

Time-division multiplexing (TDM) has been widely used in multi-channel recording where area and power are of concern [11]. Multiple channels can share a single front-end with different electrodes. A single amplifier also offers an extra benefit of uniform gain, making the gain consistent among individual channels.

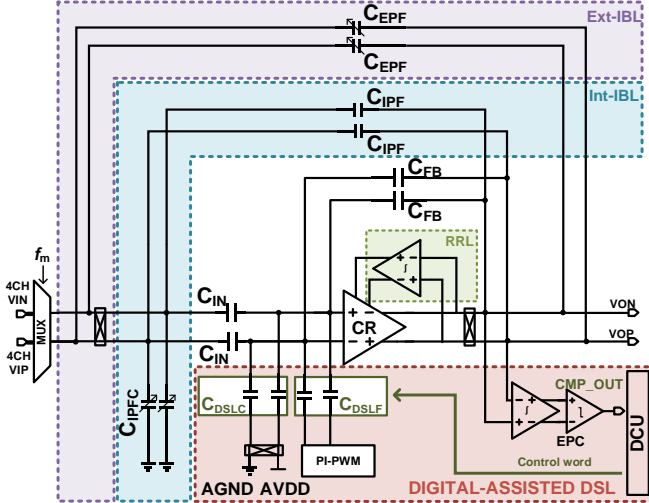


Fig. 2. TOP overview

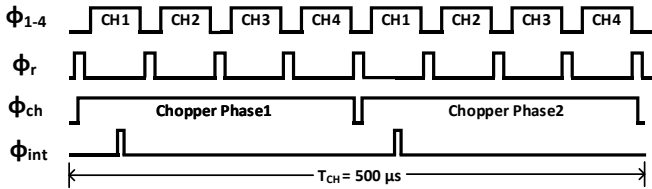


Fig. 3. Timing diagram of the TDM.

Surface electrodes are subject to large electrode offset voltages. In worst case scenarios, the dc-offset voltage of dry electrodes can be up to ± 300 mV [12]. To keep the front-end amplifier saturation free, the front-end circuit requires a large dc-suppression capability. Analog DC servo loop (DSL) (Fig. 1(c)) and mix-mode DSL [13, 14] are not suitable for a TDM-based AFE, because an integrator with an intrinsically large time constant cannot be easily toggled among individual channels. Although fully digital DSL may also be slow at the first use, but its control word can be stored for future use and the calibration is only needed when the residual dc voltage exceeds a preset threshold. Shin employed a delta-sigma CDAC to achieve a high-resolution dc suppression [15]. However, the delta-sigma CDAC requires a wide-band AFE which leads to noise folding in a TDM configuration, thus, significantly degrading the noise performance (see Fig. 1(d)).

This paper proposes a 4-channel TDM-based AFE with high input impedance of up to $83 \text{ G}\Omega$ and a dc tolerance of up to ± 384 mV while the input-referred noise is kept below $0.47 \mu\text{V}_{\text{rms}}$. This paper is organized as follows. Section II introduces the system architecture and circuit implementation of the proposed AFE. Section III and Section IV present the simulation results and conclusions, respectively.

II. CIRCUIT IMPLEMENTATION

A. System architecture

Fig. 2 shows the implementation of the proposed ear-EEG AFE composed of a TDM-based capacitively-coupled instrumentation amplifier (CCIA), two impedance boost loops

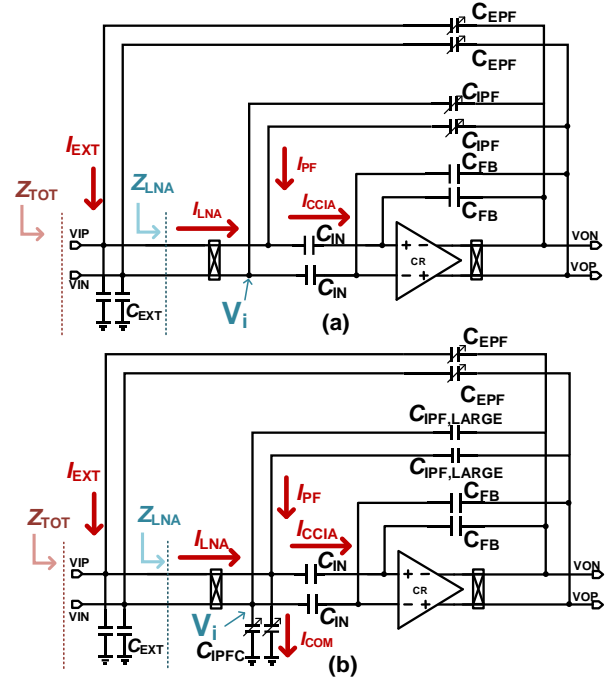


Fig. 4. (a) conventional IBL, (b) proposed Int-IBL.

(including an external IBL, i.e., Ext-IBL; and an internal IBL, i.e., Int-IBL), and a digital-assisted DC servo loop (including a coarse DSL and a fine phase-interleaving DSL (PI-DSL)). Both positive and negative inputs of the TDM-CCIA are time-division multiplexed among 4 ear-EEG recording electrodes.

The multiplexing frequency, f_m is 16 kHz (i.e., 4 kHz per channel) which is 2 times higher than the chopper frequency $f_{\text{ch}} = 2 \text{ kHz/ch}$. The input capacitors, C_{IN} , and feedback capacitors, C_{FB} , are set to 40 pF and 0.4 pF respectively, providing a gain of 40 dB . Fig. 3 shows the timing diagram of the TDM control. During ϕ_{1-4} the AFE selectively amplifies the signal from the recording electrodes 1-4, while in ϕ_r the critical nodes of the AFE are reset to the optimal common-mode voltage every time when channel switching occurs in order to reduce the crosstalk between successive channels. A current reused transconductance amplifier [13] is employed as the core amplifier to lower the thermal noise. Chopper is placed in front of the input capacitor C_{IN} to enhance the total CMRR. The -3 dB bandwidth ω_{AFE} of the AFE is set to 40 kHz in order to satisfy the setup accuracy requirement of a 10-bit ADC sampled at 16 kHz , which is given by [16],

$$\omega_{\text{AFE}} > 2 \times (10 + 1) \times 16\text{k} \times \ln 2 \quad (1)$$

B. Two-Stage-Compensation Impedance Boost Loop

Fig. 4(a) shows the structure of a conventional IBL. The total input impedance of such a circuit, Z_{TOT} , is given by

$$Z_{\text{TOT}} = \frac{1}{sC_{\text{EXT}}} \parallel Z_{\text{LNA}} \quad (2)$$

where C_{EXT} represents the lumped parasitic capacitance from the ESD pad and external interconnections, and Z_{LNA} is the input impedance of the LNA.

For the convenience of the analysis, we first neglect C_{EXT} . Fig. 4(a) illustrates all the current in the input node. The current flowing into the LNA, I_{LNA} , is given by,

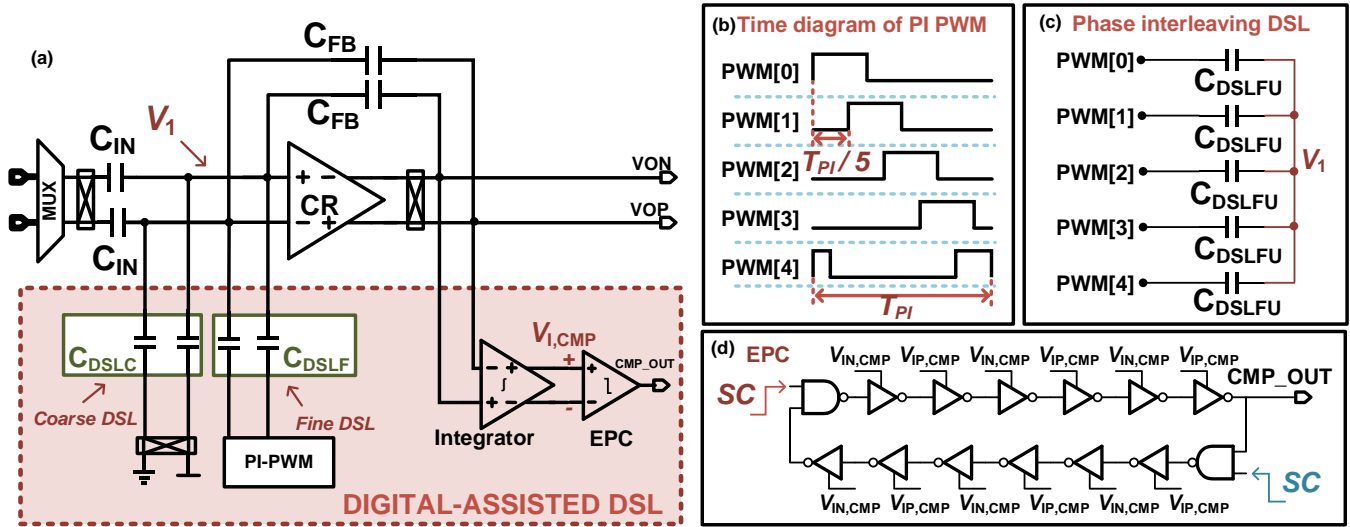


Fig. 5. Implementation of the PI-DSL.

$I_{LNA} = I_{CCIA} - I_{PF} = V_i \cdot 2f_{ch} \cdot (C_{IN} - (A_0 - 1) \cdot C_{IPF})$ (3)
 where I_{CCIA} is the current flowing into the CCIA, I_{PF} is the compensation current via C_{IPF} , I_{LNA} is the current at the input of the chopper, and A_0 is the AFE's closed loop gain. One can trim the C_{IPF} to make I_{PF} equal to I_{CCIA} . Thus, to achieve an infinite Z_{LNA} the optimal value of the positive feedback capacitor, $C_{IPF,optimal}$, should be equal to $C_{IN}/(A_0-1)$. The new Z_{LNA} after-trimming can be summarized as,

$$Z_{LNA,1} > \frac{1}{2f_{ch} \cdot (A_0 - 1) \cdot \frac{1}{2} C_{IPF,LSB}} \quad (4)$$

where $C_{IPF,LSB}$ is the LSB of the trimming capacitor array. Therefore, IBF is limited by the minimum cap size that a silicon process can achieve and the closed-loop gain of the LNA.

Fig. 4(b) shows the proposed Int-IBL. Instead of relying on an adjustable C_{IPF} to make $I_{PF} = I_{LNA}$, the proposed IBL utilizes a fixed C_{IPF} which is intentionally set to slightly larger than $C_{IPF,optimal}$. A large C_{IPF} causes an over-compensated current flowing into Node V_i . But the extra current is sunk by the 6-bit CDAC, C_{IPFC} , leading to almost zero I_{LNA} . The input current of LNA I_{LNA} is defined as,

$$I_{LNA} = I_{CCIA} + I_{COM} - I_{PF} \quad (5)$$

$$I_{LNA} = V_i \cdot 2f_{ch} \cdot (C_{IN} - (A_0 - 1) \cdot C_{IPF} + C_{IPFC}) \quad (6)$$

where I_{COM} is the compensation current flowing into C_{IPFC} . The Z_{LNA} is now boosted to,

$$Z_{LNA,2} > \frac{1}{2f_{ch} \cdot \frac{1}{2} C_{IPFC,LSB}} \quad (7)$$

where $C_{IPFC,LSB}$ is the LSB of the trimming capacitor array C_{IPFC} . Comparing (4) with (7), if the LSB of C_{IPFC} is equal to that of C_{IPF} , $Z_{LNA,2}$ is (A_0-1) times larger than $Z_{LNA,1}$. The LSB of C_{IPFC} is designed as 5 fF, therefore the theoretical maximum after-trimming input impedance is larger than 100 GΩ.

When C_{EXT} is taken into account, an additional current, I_{EXT} , is present. C_{EXT} appears as C_{EXT}/f_{ch} at node V_i (see Fig. 4(a)). Limited by the resolution of C_{IPFC} , such a small C_{EXT}/f_{ch} is difficult to compensate by C_{IPFC} alone [10]. Therefore, we place an external IBL, similar to [10], to form a negative capacitor to compensate for the C_{EXT} . The new overall input impedance of the CCIA becomes,

$$Z_{TOT} = \frac{1}{s(A_0 - 1) \cdot \frac{1}{2} C_{EPF,LSB}} \parallel Z_{LNA,2} \quad (8)$$

where C_{EPF} is an adjustable CDAC on the external IBL path, whose LSB ($C_{EPF,LSB}$) is also 5 fF. With $A_0 = 40$ dB, theoretical calculation reveals that Z_{TOT} at 100 Hz and 1 Hz are larger than 6 GΩ and 86 GΩ, respectively.

C. DC Servo Loop

The DSL is composed of a coarse DSL and a phase-interleaving DSL (PI-DSL) for fine adjustment (see Fig. 5(a)). The coarse DSL consists of a 7-bit capacitor DAC, C_{DSLFC} , with an LSB of 50 fF, and is driven by a 1.2-V square waveform. Although the maximum input-referred EDO that can be suppressed by the coarse DSL is 384 mV, which is limited by the size of the LSB capacitor, it can still leave a residual input-referred EDO of 3 mV which can be further eliminated by the fine PI-DSL.

The fine PI-DSL consists of a uniform-weighted 5-bit CDAC, C_{DSLFC} , with each capacitor being 10 fF. Unlike C_{DSLFC} , the C_{DSLFC} is driven by five phase-interleaving pulse-width-modulated (PWM) waveforms. All five PWM waveforms have the same pulse width defined by the control words from the digital control unit. Every successive PWM waveform has a phase difference of $2\pi/5$ and drives a single bit of C_{DSLFC} (see Figs. 5(b) and (c)). The period of the PWM, T_{PI} , is 1.5 μs and is quantized by a 20-MHz clock (f_{clk}). The DC component of the PWM signals suppresses the EDO. Therefore, every LSB of the fine DSL can suppress an EDO of 100 μV. The charges from the five PI-PWM waveforms are summed in C_{FB} . The harmonic frequencies of the PI-PWM waveforms are up modulated by a factor of 5, which can easily be removed by the intrinsic low-pass characteristic of the LNA.

Since the EDO changes slowly over time, an integrator with a cut-off frequency of 50 mHz is used to monitor the DC component of the LNA's output. An edge-pursuit comparator (EPC) similar to [17] quantizes the residue EDO. If the residual EDO is larger than one LSB of the PI-DSL, one increment or decrement is made to the existing code of the DSL according to the EPC's output. Fig. 5(d) shows the structure of the EPC,

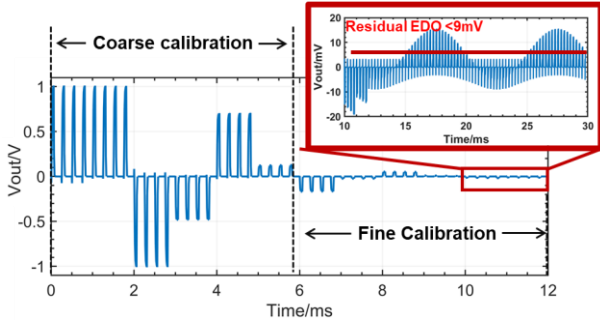


Fig. 6. Timing diagram for calibration

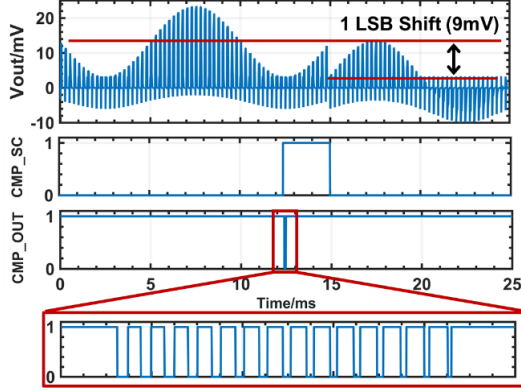


Fig. 7. Timing diagram for monitoring residual EDO.

which consists of two NAND gates and two 6-stage inverter cells. At the beginning, the START_COMPARE signal (SC) is low and no power is consumed. Once the SC goes high, two edges start to progress along the inverter chains. As the progression speed of the two edges are determined by the differential inputs to the EPC, i.e., $V_{IP,CMP}$ and $V_{IN,CMP}$ (see Fig. 5), the two edges travel at different speeds until one overtakes the other. The time for the EPC to complete one comparison is determined by the amplitude of the EPC's inputs.

Therefore, there is an inherent coarse quantization capability in the EPC, which can be used to quantize and monitor the residual EDO. The relationship between $|V_{IP,CMP} - V_{IN,CMP}|$ and EPC output's (CMP_OUT) is given by

$$N = \frac{I_B}{2g_m V_{LCMP}} \quad (9)$$

where N is number of oscillation cycles in the CMP_OUT signal during the ON-phase of the CMP_SC, I_B is the bias current of the EPC, g_m is transconductance of the EPC's input transistor. N is sensitive to PVT variations as V_{LCMP} is proportional to the open loop gain, A_{INT} , of the integrator. Therefore, each chip will have a chip-specific digital code, N_{LF} , where N_{LF} is the monitoring threshold of the residual DC voltage.

Every channel is calibrated once. Then, in the operation mode, the EPC samples the residual DC voltage at the LNA's output every 8 seconds. Only when the measured N is smaller than N_{LF} , the fine PI-DSL will increase or decrease by one LSB depending on the output of the EPC. Fig. 6 shows the timing diagram for the proposed DSL's calibration. A bit shift of the DSL occurs when the residual EDO is larger than the threshold (see Fig. 7).

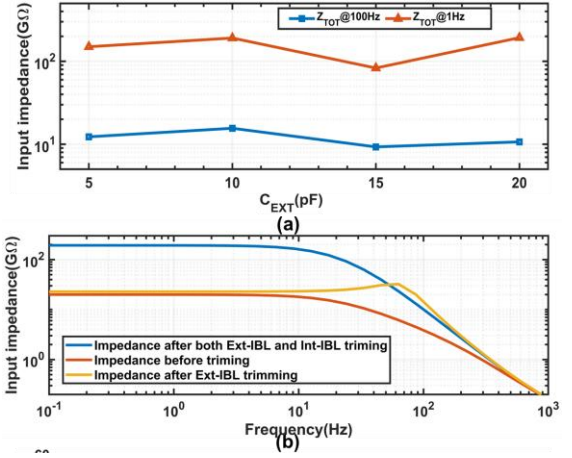


Fig. 8(a) Simulated input impedance at different frequencies with different C_{EXT} (b) Simulated input impedance with $C_{EXT}=20$ pF.

Table I. PERFORMANCE & COMPARISON

	[14] JSSC 18	[11] JSSC22	[16] JSSC22	This work^a
Process	65nm	110nm	65nm	180nm
Supply(V)	1.2	1	1.2	1.2
Power/Ch	4.5 μ W	3.8 μ W	0.7 μ W	5.4μW
INR(μ V _{rms})	0.38	0.36	3.2	0.47
BW (Hz)	0.5-100	0.5-300	1-500	0.5-100
NEF	3.32	4.65	-	2.69
Z_{IN} (Ω)	-	15G	24.5M	>83GΩ^b
EDO(mV)	350	-	50	384

^a Simulated Result ^b Z_{in} @ 1 Hz

III. SIMULATION RESULT

The proposed AFE has been validated in the Cadence Virtuoso Environment using X-FAB's 0.18- μ m CMOS process. The AFE consumes 18 μ A under a 1.2-V supply. Fig. 8(a-b) shows the simulated input impedance of the AFE under different conditions. It is evident that even with $C_{EXT} = 20$ pF, the simulated input impedance is still higher than 9.3G Ω at 100 Hz and higher than 83G Ω at 1Hz. Fig. 8(c) shows the simulated input-referred noise (IRN) of the AFE. The INR from 0.5-100 Hz is 0.47 μ V_{rms} at the presence of 384mV EDO. Table I shows the performance summary of the proposed AFE and how it compares to the state-of-the-art. The proposed AFE achieves the highest input impedance and large EDO tolerance while maintaining a comparable NEF to the state-of-the-art designs.

IV. CONCLUSION

A TDM-based AFE suitable for ear-EEG recording is proposed. Thanks to the novel impedance boost loops and phase-interleaving DC servo loop, the AFE achieves an ultra-high input impedance of 83 G Ω and large EDO tolerance up to ± 384 mV.

REFERENCES

- [1] R. Kaveh, J. Doong, A. Zhou, C. Schwendeman, K. Gopalan, F. L. Burghardt, A. C. Arias, M. M. Maharbiz, and R. Muller, "Wireless User-Generic Ear EEG," *IEEE Trans Biomed Circuits Syst*, vol. 14, no. 4, pp. 727-737, Aug, 2020.
- [2] D. Looney, P. Kidmose, C. Park, M. Ungstrup, M. Rank, K. Rosenkranz, and D. Mandic, "The in-the-ear recording concept: user-centered and wearable brain monitoring," *IEEE Pulse*, vol. 3, no. 6, pp. 32-42, Nov-Dec, 2012.
- [3] A. Stochholm, K. Mikkelsen, and P. Kidmose, "Automatic Sleep Stage Classification Using Ear-EEG," *2016 38th Annual International Conference of the Ieee Engineering in Medicine and Biology Society (Embc)*, pp. 4751-4754, 2016.
- [4] C. B. Christensen, J. M. Harte, T. Lunner, and P. Kidmose, "Ear-EEG-Based Objective Hearing Threshold Estimation Evaluated on Normal Hearing Subjects," *IEEE Trans Biomed Eng*, vol. 65, no. 5, pp. 1026-1034, May, 2018.
- [5] Y. J. Kim, N. S. Kwak, and S. W. Lee, "Classification of Motor Imagery for Ear-EEG based Brain-Computer Interface," *2018 6th International Conference on Brain-Computer Interface (Bci)*, pp. 129-130, 2018.
- [6] S. I. Choi, C. H. Han, G. Y. Choi, J. Shin, K. S. Song, C. H. Im, and H. J. Hwang, "On the Feasibility of Using an Ear-EEG to Develop an Endogenous Brain-Computer Interface," *Sensors (Basel)*, vol. 18, no. 9, Aug 29, 2018.
- [7] S. L. Kappel, M. L. Rank, H. O. Toft, M. Andersen, and P. Kidmose, "Dry-Contact Electrode Ear-EEG," *IEEE Trans Biomed Eng*, vol. 66, no. 1, pp. 150-158, Jan, 2019.
- [8] Q. Fan, F. Sebastiano, J. H. Huijsing, and K. A. A. Makinwa, "A 1.8 μ W 60 nV/ $\sqrt{\text{Hz}}$ Capacitively-Coupled Chopper Instrumentation Amplifier in 65 nm CMOS for Wireless Sensor Nodes," *IEEE Journal of Solid-State Circuits*, vol. 46, no. 7, pp. 1534-1543, 2011.
- [9] U. Ha, and H.-J. Yoo, "An EEG-NIRS ear-module SoC for wearable drowsiness monitoring system," in *2016 IEEE Asian Solid-State Circuits Conference (A-SSCC)*, 2016, pp. 193-196.
- [10] Y. Park, J.-H. Cha, S.-H. Han, J.-H. Park, and S.-J. Kim, "A 3.8- μ W 1.5-NEF 15-G Ω Total Input Impedance Chopper Stabilized Amplifier With Auto-Calibrated Dual Positive Feedback in 110-nm CMOS," *IEEE Journal of Solid-State Circuits*, vol. 57, no. 8, pp. 2449-2461, 2022.
- [11] K. J. Choi, and J. Y. Sim, "An 18.6- μ W/Ch TDM-Based 8-Channel Noncontact ECG Recording IC with Common-Mode Interference Suppression," *IEEE Trans Biomed Circuits Syst*, vol. PP, Dec 16, 2022.
- [12] J. Xu, S. Mitra, C. Van Hoof, R. F. Yazicioglu, and K. A. A. Makinwa, "Active Electrodes for Wearable EEG Acquisition: Review and Electronics Design Methodology," *IEEE Rev Biomed Eng*, vol. 10, pp. 187-198, 2017.
- [13] J. Lee, K.-R. Lee, U. Ha, J.-H. Kim, K. Lee, S. Gweon, J. Jang, and H.-J. Yoo, "A 0.8-V 82.9- μ W In-Ear BCI Controller IC With 8.8 PEF EEG Instrumentation Amplifier and Wireless BAN Transceiver," *IEEE Journal of Solid-State Circuits*, vol. 54, no. 4, pp. 1185-1195, 2019.
- [14] Y. Park, S. H. Han, W. Byun, J. H. Kim, H. C. Lee, and S. J. Kim, "A Real-Time Depth of Anesthesia Monitoring System Based on Deep Neural Network With Large EDO Tolerant EEG Analog Front-End," *IEEE Trans Biomed Circuits Syst*, vol. 14, no. 4, pp. 825-837, Aug, 2020.
- [15] U. Shin, C. Ding, B. Zhu, Y. Vyza, A. Trouillet, E. C. M. Revol, S. P. Lacour, and M. Shoaran, "NeuralTree: A 256-Channel 0.227- μ J/Class Versatile Neural Activity Classification and Closed-Loop Neuromodulation SoC," *IEEE J Solid-State Circuits*, vol. 57, no. 11, pp. 3243-3257, 2022.
- [16] H. Jiang, S. Nihtianov, and K. A. A. Makinwa, "An Energy-Efficient 3.7-nV/ $\sqrt{\text{Hz}}$ Bridge Readout IC With a Stable Bridge Offset Compensation Scheme," *IEEE Journal of Solid-State Circuits*, vol. 54, no. 3, pp. 856-864, 2019.
- [17] M. Shim, S. Jeong, P. D. Myers, S. Bang, J. Shen, C. Kim, D. Sylvester, D. Blaauw, and W. Jung, "Edge-Pursuit Comparator: An Energy-Scalable Oscillator Collapse-Based Comparator With Application in a 74.1 dB SNDR and 20 kS/s 15 b SAR ADC," *IEEE Journal of Solid-State Circuits*, vol. 52, no. 4, pp. 1077-1090, 2017.